# Kinematic interpretation of the 3D shapes of metamorphic core complexes

Laetitia Le Pourhiet, Benjamin Huet, Dave May, Loic Labrousse, Laurent Jolivet

# Kinematic interpretation of the 3D shapes of metamorphic core complexes

Submitted to G-cubed

Authors:

**Laetitia Le Pourhiet** [1,2]

**Benjamin Huet** [3]

**Dave A. May** [4]

**Loic Labrousse** [1,2]

**Laurent Jolivet** [5]

Affiliations:

*1 UPMC Univ Paris 06, UMR 7193, ISTEP, F-75005, Paris, France.*

*2 CNRS, UMR 7193, ISTEP, F-75005, Paris, France*

*3 Department for Geodynamics and Sedimentology, University of Vienna, Althanstrasse 14 A-1090 Vienna*

*4 Institute of Geophysics, Department of Earth Sciences, ETH Zurich, Switzerland*

*5 ISTO, Université d'Orléans-CNRS, UMR 6113, F-45071 Orléans, France*

**Abstract**

**Metamorphic Core Complexes form dome shaped structures in which the ductile crust is exhumed beneath a detachment fault. The 3D dome geometry, inferred by mapping the schistosity in the exhumed crust, can be either elongated normal to the stretching direction or along it. In the first case, the domes are interpreted as having formed during extension. However, in the second case, they are interpreted either as strike-slip, transpressive or constrictive extensional structures, depending on the geodynamic context. Numerical models of metamorphic core complexes published to date are all two-dimensional and therefore, theoretically only apply to domes which are elongated normal to the stretching direction. Here, we explore by means of 3D thermo-mechanical modeling, the impact of 3D kinematic extensional boundary conditions on the shape of metamorphic core complexes. We examine the impact of a transtensional step over and of horsetail splay fault kinematics on the dynamics of exhumation, finite strain and P-T paths, and compare them to cylindrical 3D models. We show, for the first time, that domes formed in transtensional step over, or at the tip of propagating strike-slip faults, display a finite strain field which can be interpreted as characteristic of a transpressive domes, although no shortening was applied in the far-field. Applying our models to the Cyclades, we propose that the coeval formation of domes elongated normal and parallel to the stretching during the Miocene can be the result of horsetail splay fault kinematics, which could correspond to the formation of a tear in the Aegean slab.**

# 1 Introduction

Metamorphic Core Complexes (MCCs) form dome shaped structures of metamorphic rocks exhumed from the middle to lower crustal depth under a detachment fault. These domes are present in many post-orogenic contexts. The dome axis, which is recognized by mapping the schistosity pattern in the exhumed metamorphic rocks, can either be elongated parallel to the stretching lineation (a-type domes Figure 1, orange structure), or normal to this direction (b-type domes Figure 1, blue structure). In the first case, the schistosity strikes mainly parallel to the direction of stretching while in the second case it strikes normal to it. Hence, b-type domes are cylindrical structures and may be modeled in 2D plane strain cross-section while the a-type domes are intrinsically 3D structures since local horizontal constriction occurs normal to stretching. This a-type versus b-type classification, first defined in Jolivet et al. [2004] based on Mediterranean examples, relies on a quantitative description of the finite-strain field. The interpretation of these structures in terms of larger scale kinematics is an ill posed inverse problem, which reaches by definition, a non-unique answer.

Structural geologists generally unambiguously interpret b-type domes as the mark of extension. This interpretation could be questioned, however, since the structure is cylindrical, it constitutes the simplest conceptual model. The Bitterroot Eocene core complex in the Northern Rockies, Idaho [*Hyndman, 1980*] and the North Cyclades Detachment System (NCDS), Greece [*Jolivet et al., 2010*] constitutes a set of excellent natural examples of b-type structures, although in both cases, strike-slip faults are inferred in the vicinity of these domes [*Foster et al. 2007; Philippon et al. 2012*].

However, the kinematic interpretation of a-type domes is not straightforward and depends on the geodynamic context. In some cases like Kesebir-Kardamos, Bulgaria *[Bonev et al., 2006*], Buckskin Rawhide, Harcuvar; Arizona, US [*Reynolds and Spencer,1985; Howard and John 1987*], Naxos, Greece [*Kruckenberg et al., 2011*] or the Western Gneiss Region, Norway [*Labrousse et al. 2004*], the domes are mainly associated to extension with a slight component of strike-slip in the kinematics. In other cases, these domes are principally associated with strike-slip kinematics with a component of transtension like the Dai Nui Con Voi dome, Vietnam, [*Jolivet et al., 2001*] or a component of transpression like along the Red River Fault system [*Leloup et al., 1995*]. However, in the Betics Cordillera [*Martinez-Martinez et al. 2002; Augier et al. 2005*] or in the Variscan orogeny (e.g. Montagne noire, France, [*Echtler et Malavielle, 1990*]), the large-scale kinematics that accompanies their formation is deeply debated. Whether these structures are interpreted as the result of shortening followed by perpendicular stretching, of coeval stretching and lateral shortening, or of pure strike-slip wrenching changes the interpretation of these structures in term of the large scale kinematics at the time of their formation.

Since Buck [*1991*], MCCs are known to form in a local extensional setting when the viscous diffusivity of the flow in the lower crust is small, i.e. when lower crust is thick and/or weak. Several processes leading to either, or both, of these conditions have been proposed and modeled: (i) thermal equilibration of a thickened crust at high Moho temperatures [*Gaudemer et al., 1988; Block and Royden, 1990; Tirel et al., 2008; Tirel et al., 2009*], (ii) partial melting of the lower crust [*Lister and Baldwin, 1993; Vanderhaeghe and Teyssier, 2001; Rey et al., 2009*],

(iii) adjunction of water [*McKenzie and Jackson 2002*] or (iv) underthrusting of weaker units below stronger ones prior to extension [*Huet et al. 2011a, 2011b*]. All the models stated above only accounted for cylindrical structures and therefore are theoretically only applicable to b-type domes.

Here, we first attempt to understand the impact of 3D kinematic extensional boundary conditions on the 3D geometry of MCCs, i.e. the relative geometry of the schistosity pattern versus the stretching lineation pattern within the exhumed crust. In the second part of the paper, we compare the results of the model to the MCCs of the Cyclades, which provides examples of the two types of domes formed during the same, well constrained, geodynamic event. Lastly we draw more general conclusions about the kinematic implications of the observation of a-type domes.

# 2 Modeling approach

## 2.1 Choice of initial conditions

The models have a fixed sized geometry of 200 x 200 x 100 km and evolve in time for 12 Myr, with a constant extension rate of 1cm/yr. Given the assumed size and the grid resolution (3 km) of the models, we expect to resolve the first order impact of large scale, 3D kinematic constraints. The models consist of three horizontal layers (See Figure 2 for the vertical profile).

Since the thermo-mechanical initial conditions for forming MCCs are well understood from 2D modeling, and our study focus on the impact of 3D boundary conditions on their resulting shape, the model design accounts for most of the factors that are known to favor the occurrence of MCCs. This includes an initially thickened crust of 50km [*Buck 1991, Gaudemer et al. 1988, Block and Royden, 1990*] and an initial thermal gradient which is set to 17.5°C/km.

104 We note that this gradient yields a Moho temperature of 875°C, which is higher than the 800°C
105 limit proposed by Tirel et al. [*2008*]. At asthenospheric depth, the initial temperature is clamped
106 not to exceed 1300°C (Figure 2). The crust itself consists of two layers of 25 km each. At a given
107 temperature, the top layer (brown shades, Figure 2) is mechanically stronger than the lower one
108 (blue shades, Figure 2), imposing a step in the strength profile at the interface between the two
109 layers. These models thus resemble the set up of the pioneering analogue models of MCCs [*Brun*
110 *et al. 1994*], except they account for the re-strengthening of material as it gets exhumed and
111 cools.

112 The initial weakness of the lower layer can be equally interpreted as the result of
113 adjunction of water in the lower crust [*McKenzie and Jackson 2002*], as the occurrence of partial
114 melt in the lower crust [*Lister and Baldwin, 1993; Rey et al., 2009*] or as the presence of under-
115 plated soft sediments or continental upper crust [*Huet et al. 2011a*]. We do not dismiss that the
116 formation of MCCs can be of diapiric nature [*Lister and Baldwin, 1993*], however, in order to
117 keep the model general, we assign a constant density to the whole crust of 2800 $kg.m^{-3}$ so that
118 buoyancy forces are limited to those arising from the thermal expansion coefficient which is set
119 constant to $3x10^{-5}$ $K^{-1}$.

120 **2.2 Treatment of the rheology**

121 At the scale of these models, the rheology in any given volume has no reason to be one of
122 pure quartz, pure olivine or plagioclase and must be influenced by the layering of the rocks, their
123 anisotropy, structural softening and hardening due to small scale boudinage and folding. In
124 practice it is not yet possible to account for all this complexity in crustal or lithospheric scale
125 modeling. As the viscous strength of rock depends to first order on temperature, we approximate

it by a Newtonian flow rule based on Frank-Kamenetskii, for which we need to provide two parameters, a reference viscosity $\eta_0$ and a characteristic temperature $\theta^{-1}$, in order to compute the effective viscosity,

$$\eta_{eff} = \eta_0 e^{-\theta T} \quad (1)$$

At high stress, this viscosity is lowered by the action of a Drucker Prager visco-plastic flow rule such that

$$\eta_{eff} = \frac{1}{2}\frac{\sigma^y}{\dot{\varepsilon}^{II}}, \quad (2)$$

where $\dot{\varepsilon}^{II} = 1/2\sqrt{\dot{\varepsilon}_{ij}\dot{\varepsilon}_{ij}}$ is the second invariant of the strain rate tensor ($\dot{\varepsilon}_{ij}$) and the yield stress, $\sigma^y$, depends on pressure $P$ and plastic strain $\varepsilon^p$ accumulated by the particles following

$$\sigma^y = P\sin\phi(\varepsilon^p) + C_0\cos\phi(\varepsilon^p). \quad (3)$$

Accounting for plastic strain softening is necessary [*Lemiale et al. 2008*] to localize plastic shear bands in visco-plastic codes such as GALE [*Moresi et al 2003*]. We impose softening on friction in the upper and lower crust with a friction angle decreasing from 30° to 10° with plastic strain varying from 0 to 20%, given the element size (3km), softening is therefore achieved for a displacement of 500 m in nature.

The rheological parameters used for the study are listed in Table 1 and were chosen because they resulted in a yield strength envelope similar to pre-existing 2D models of Huet et al. [*2011a*], thereby allowing us to verify (or benchmark) our results with pre-existing models run with a other numerical code, namely FLAMAR [*Yamato et al. 2007*]. In the parameterization, we have chosen to keep $\eta_0$ constant and to vary the characteristic temperature $1/\theta$. This choice was governed by the idea that when the temperature is zero at the surface, both

147 the lower and upper crust must have the same effective viscosity in order to enable yielding.
148 However, with this choice, the viscosity of the lower crust may drop to a non-realistic value at
149 the base of the lower crust. Therefore we adopted a lower cut-off for the viscosity in the models,
150 which we set to $10^{19}$ Pa.s, as in previously published 2D models [*Huet et al. 2011a, Tirel et al.*
151 *2008*].

152 The previous study by Huet et al. [*2011a*] investigated the role of the rheological
153 layering and temperature on the distribution, or localization of the deformation without imposing
154 a priori the location of faults. To avoid strain localization on the side of the box, they used
155 random damage all through the upper crust except in the vicinity 30 km from the boundary. The
156 model domain was longer and show that with a 25 km thick brittle crust, strain started to localize
157 by distributed necking with a wavelength of 70 km. Depending on the rheological layering of the
158 crust, either the strain remained distributed and no exhumation of lower crust was occurring or
159 only one of the initial grabens was still active after 2 Myr before turning into a MCC. In the
160 present study, we investigate the role of 3D kinematics on the shape of MCC. We have therefore
161 chosen a rheological layering which favor their formation and imposed a 50 km wide zone with
162 random pre-existing damage in the center of the model to avoid unwanted border effects.

163 **2.3 Numerics**

164 All the numerical experiments were run with GALE 1.6.1, an open source code, which
165 solves incompressible Stokes flow coupled with heat conservation via a finite element, particle-
166 in-cell method in three dimensions [*Moresi et al., 2003*]. The computational mesh consisted of
167 64x64x32 Q1 (trilinear) elements. Evolution in time is obtained through advection of particles

(tracking lithology) and the thermal energy equation, with time steps limited to 10% of Courant criterion.

As GALE uses Q1Q1 elements, it is necessary to scale the viscosity of the model to be close to one in order to obtain accurate results and convergence. The scaling used to run the code is provided in Table 2. Additional passive markers have been included to compute the finite strain field in the lower crust and to track P-T paths. An Octave script used for post-processing the finite strain ellipsoid and exporting it into a VTK format for visualization purpose are included as supplementary material. The method used to compute the finite strain tensor in 3D from passive markers is detailed in appendix A.

Each run consists of 200-300 time steps, requiring approximately 72 hr of computation using a parallel geometric multi-grid (GMG) solver on 16 CPU (dual core AMD Opteron 2.6 GHz, each with 1 GB of RAM). A full description of the multi-grid method used in GALE is provided in Appendix B. We refer the reader, who would like to reproduce the results or reuse the input files, to the supplementary material. It includes the input files of the models, solver options and patches for GALE to reproduce the specific boundary conditions and viscous cutoff implemented for this study.

## 3 Impact of boundary conditions on the shape of MCCs

Three types of extensional boundary conditions are considered. The boundary conditions are represented by black arrows that indicate the velocity applied on the front (pink) and back (cyan) boundaries of the models (Figure 3a). First, 3D cylindrical extension is applied by imposing a constant normal velocity on one side of the model (the cyan boundary, Figure 3a and 4). This model is used both for verifying the modeling approach as compared to existing 2D

models and to compare the results with a non-cylindrical, 3D boundary conditions. The second model considers extension occurring at an extensional step-over between two left lateral strike-slip faults applied on the front (pink) and back (cyan) boundaries of the model (Figure 3b and 5). The third model considers the case of a transtensional fault propagator which accommodates a left-lateral step in the rate of extension at the front of the model (pink) (Figure 3c and 6). The two lateral boundaries are free-slip boundaries.

### 3.1 Surface deformation

The surface deformation pattern after 12 Myr of extension is outlined in map view, by the light brown stripes, which were originally forming square (Figure 3). The most striking feature at that point is that the cylindrical and the fault propagator kinematics lead to the exhumation of deep crustal material to the surface (blue material on Figure 3a, 3c), whilst the step-over kinematics model does not (Figure 3b). In the case of cylindrical boundary conditions (Figure 3a), the model produces one structure, elongated normal to the direction of stretching. In the case of fault propagator kinematics, the initially deep crustal material is exhumed along a curvilinear trend which follows the fault propagator and turns to become orthogonal to the free slip side of the model. This trend is therefore parallel to the stretching direction close to the back boundary, whereas it is perpendicular to the stretching direction close to the left hand side boundary. Looking in more detail, one sees that in between the two branches, there are less exhumed rocks and that the strike-slip part appears to be elongated further towards the back of the model than the location of the cylindrical part of the exhumed structure (Figure 3c).

### 3.2 Topography

Colored isolines indicate the surface topography (Figure 3). All the models produce

relatively low topographic expression with an altitude ranging from -800 m to 800 m for the model 1 (Figure 3a), from -1200m to 1000m for model 2 (Figure 3b) and from -1200 m to 1300 m for model 3 (Figure 3c). The exhumed deeper crustal rocks tend to be located below topographic lows rather than beneath the topographic highs. Noticeably, the two models with a strike-slip component produce significantly more topographic expression than the cylindrical model. The steepest gradients are observed along the strike-slip faults. Along the front side, the topography may be over estimated due to border effects, but in the center of the model, the topographic gradients remains significant. In the regions exhibiting strike-slip deformation, the topographic lows tend to be aligned in the direction of stretching. Comparing the cylindrical model (Figure 3a) with the cylindrical part of the fault propagator model (Figure 3c), the presence of the strike-slip fault changes the geometry of topography, since a secondary topographic low that is absent from the purely cylindrical model appears.

### 3.3 3D-geometry and finite-strain inside the domes

Along cross-sections through all the models, one sees that the Moho remains strikingly flat (Figure 4, 5 and 6) while the deeper, ductile, part of the crust is exhumed within dome shaped structures, even in model 2 where it does not reach the surface. The finite strain field calculated locally in the lower crust is represented by the stretching lineation superposed to the geometry of the models (cylinders colored in function of the strike of the lineation). The lineation and the pole of the schistosity are also plotted on stereo-diagrams.

In the case of cylindrical extension (Figure 4), the dome is approximately symmetric and elongated normal to the stretching direction. The detachment fault at the top of the lower crust is outlined by nearly horizontal lineations parallel to the stretching direction (Figure 4a and red dots

234 on Figure 4b), whilst vertical lineations delineate the deep core of the dome. The poles of the
235 schistosity are aligned on a vertical great circle parallel to the stretching direction (black dots on
236 Figure 4b). This pattern reflects the cylindrical nature of the dome. However, a few vertical
237 schistosity planes that strike parallel to the stretching direction mark local constriction. The
238 similarity between this cylindrical model and the 2D models on which we have based the model
239 set up [*Huet et al., 2011a*] provides confirmation that although the models were run with a lower
240 resolution in 3D, the first order kinematics is maintained. The dome formed in this simulation
241 displays all the characteristics of a b-type dome.

242 The extensional step-over kinematics (Figure 5) leads to the localization of a dome in the
243 center of the model. In this simulation, the deeper ductile part of the crust is exhumed with the
244 shape of a dome beneath the topographic depression formed by normal and strike-slip faults in
245 the upper brittle part of the crust. This dome is elongated in the direction of stretching imposed
246 from the boundary condition. It is a non-cylindrical structure because the lineations (Figure 5a)
247 are pointing out of plane when considering a cross section taken normal to the elongation of the
248 dome. The lineations (red dots Figure 5b) within the dome are systematically horizontal and the
249 schistosity planes (black dots Figure 5b) are approximately vertical, except at the very top of the
250 dome forming an antiform structure. The particles show that this structure is slightly asymmetric
251 with its steepest dipping limb located on the side of the strike-slip fault.

252 In this simulation, the strain is highly partitioned with depth. In the upper crust, the
253 deformation takes place along steep grabens or pull apart basins (Figure 3b) which reflects the
254 extensional nature of the boundary conditions. However, in the deeper part of the crust, the
255 lineation forms a horizontal sigmoid compatible with pure left-lateral deformation, while the

ductile exhumed lower crust within the dome deforms by constriction and forms an antiform (Figure 5a-b). The deformation in the exhumed part of the deeper crust is characteristic of an a-type dome (Figure 1) with a strong local component of constriction, which was not imposed in the boundary conditions (Figure 3b). Dynamically, the formation of this structure is due to the local depression that forms above the extensional step-over. The large topographic gradient drives the flow in the ductile crust, attracting it towards the pull apart, where it rises to form the dome. As the dome grows, the strength of the upper crust drops locally, leading to strong strain localization.

The fault propagator kinematics (Figure 6) display the formation of two independent domes linked by a transfer zone. The first dome forms along the gray boundary with an almost cylindrical shape, similar to the dome of Figure 4a, although the lineations at the front of the structure are slightly oblique to the stretching direction (indicated by yellow colored cylinders instead of gray cylinders). The second dome forms at the location of the imposed strike-slip boundary condition. As for the a-type dome of Figure 5a, the structure is an asymmetric fold with a steeper dipping limb close to the fault. However, the lineations in the deeper part of the crust (Figure 6a) tend to strike oblique to the direction of stretching by an angle of 25 to 50° (red dots on Figure 6b) and indicate that this dome has been fed from both the back (cyan) and the right (black) side of the model.

This model with mixed boundary condition shares many common characteristics with model 1 and 2. However, in this mixed mode, the orientation of the stretching lineation in the first 10 km of the crust is much more spread out than for purely a- or b-type domes. In this mixed mode, the azimuth of the lineation may locally rotate by 40-50° as compared to the

direction of extension or shear imposed from the boundary conditions.

### 3.4 P-T paths

The computation of synthetic P-T paths is common practice to validate models with observations in orogenic settings [*Gerya et al. 2000, Yamato et al. 2007*]. In both the case of the cylindrical and the fault propagator models (Figure 4c, 6c), despite the rather different shape of the domes in map view and the different kinematic imposed at the boundary, the P-T paths recovered from the two models are very similar. In both cases, the rocks are exhumed from all depths along the initial thermal gradient of 17°/km and starting from there, the exhumation takes place along isothermal or slightly heating P-T paths. In both models the final cooling of the exhumed rocks follows a linear gradient of c.a. 50°C/km which reflects the thinning of the crust. P-T paths of the step-over model (Figure 4c) contrast with the first two. They do not display heating P-T paths, and the decompression arises with significant cooling. The thermal gradient after 12 Myr reaches only 33°/km as a result of the relatively small amount of thinning of the lower crust involved in these models as compared to model 1 and 3.

## 4 Summary and discussion of modeling results

### 4.1 Impact of initial conditions

An important feature of all these models is the rheological step that was introduced at mid crustal level. As discussed earlier, this step may represent a change in lithology due to nappe stacking as in Huet et al. [*2011a; 2011b*], or could be caused by the presence of fluid [*McKenzie and Jackson 2002*] or be the limit of partially molten crust [*Lister and Baldwin, 1993; Vanderhaeghe and Teyssier, 2001; Rey et al., 2009*]. This step in viscosity is important for the outcome of the models as it allows localizing the deformation on a single detachment zone as shown and

300 discussed in detail in Huet et al. [*2011a*] and it facilitates the rise of ductile material beneath the
301 pull-apart in model 2. Similarly, we did not explore the effect of the initial depth of the step in
302 viscosity, but we contend it would affect the initial spacing of the faults and therefore potentially
303 change the outcome of the models by increasing the number of domes if the step was located at a
304 shallower depth [*Bullard, 1936; Vening Meinesz, 1950; Spadini et Podladchikov, 1996*]. If this
305 step was to be at a lower depth, several domes would probably form initially, but at larger strain
306 one would localize strain more efficiently [*Lavier et al., 2000*; *Wijns et al., 2005*]. If several
307 steps were to be included, we can predict that the localization of the deformation would probably
308 jump from the deepest one to the shallower one over time as was observed in Huet et al. [*2011a*]

309 **4.2 Rate of extension versus rate of exhumation**

310 We observe that the model with transtensional splays (model 3, Figure 6c) exhumes lower
311 crustal rocks to the surface along warmer geothermal gradients compared to pull-apart models
312 (model 2, Figure 5c) for the same rate of extension. Part of this discrepancy is due to a
313 geometrical effect of the design of the model because the pull-apart modelled here is *infinite* and
314 therefore the source of material is limited to the left and right side, whilst in the case of a splay
315 fault, significant amount of material is pumped from the back side (cyan side, Figure 6) of the
316 model. Moreover, as the crust thins much more in the case of a splay fault (Figure 6) than in the
317 case of a pull-apart, and considering that the strength of the lower crust or the mantle is not
318 sufficient to maintain steps in the Moho, the lower crustal material located on the side with no
319 extension is forced to flow towards the a-type structures. The second reason for the discrepancy
320 is that as the dome gets wider, the diffusivity of the flow entering the a-type part of the dome
321 increases as the cube of the thickness of the channel [*Buck, 1991*], enhancing exhumation rates.

One may also question the effect of changing the rate of extension on the outcome of our models. Based on analogue models of sand and silicone putty, Brun et al. [*1994*] and Brun [*1999*] suggested that increasing the rate of extension decreases the rate of exhumation. This rate dependence is mainly due to viscous coupling which competes with the diapiric ascent of light silicone putty into the sand. As it was discussed in *Wijns et al.* [*2005*], the change of the exhumation rate observed in analogue models is largely reduced when the buoyancy forces are small, which is the case in the model presented in this paper where buoyancy forces are kept to minimal and most of the exhumation is kinematically driven. Therefore, if one would decrease the extensional velocity, the rate of exhumation would probably decrease (but not drastically), in response to both kinematic forcing and reduced buoyancy forces in response to cooling by diffusion. The P-T paths would reach a cooler final thermal gradient, but as the rheological step remains, the overall kinematics would not change drastically. Similarly, increasing the rate of extension would probably increase the rate of exhumation and render the P-T path warmer in response to increased buoyancy forces, as was observed in models including melts [*Rey et al., 2009*]. In any case, the structures and their orientations, which are central to our analysis, would remain unchanged. The presence of the rheological step thus render the overall model kinematics, or finite strain pattern, almost independent of the rate of extension.

**4.3 Significance of a-type domes**

We did not manage to create a-type domes with purely cylindrical boundary conditions, even though local components of constriction were observed in model 1. We note however that this could be an issue with the numerical grid resolution used in these models. It is possible that a-type structures could form at segments of the boundaries between domes if we considered

similar instabilities as the one proposed by Gerya [*2010*] for the formation of transform faults at mid oceanic ridges. We can also posit that similar dome shapes would occur if we had imposed the formation of two offset domes in the initial conditions such as those used in [*Choi et al., 2008; Allken et al. 2011*].

In any case, this does not contradict the main conclusion of our modelling study: when a transtensional strike-slip component is involved in the deformation of hot post-orogenic (i.e. previously thickened) crust, a-type domes form. The most important result is that the constrictive ductile deformation within these domes is the mark of strike-slip transtensive faulting in the upper crust, rather than shortening normal to the stretching direction. We agree that at a first glance these structures resemble folds, however, the contact between the upper and the lower units is used as a detachment fault to exhume deeper units within the dome. Finally, the modelled topographic pattern indicates that sedimentary basin should form on the lateral side of a-type domes.

## 5 Comparison of the models to the Aegean MCCs

The Aegean Sea is a post-orogenic domain thinned in the back arc of the Hellenic subduction zone [*Le Pichon and Angelier, 1981*]. In the Cyclades, the two types of Metamorphic Core Complexes have been exhumed with Naxos and Tinos being considered as representative of a-type and b-type domes, respectively [*Jolivet et al., 2004*] (Figure 7a). In this section, we discuss the applicability of our models to this domain and the implications for our understanding of the Aegean dynamics.

The P-T paths obtained are not sufficiently different from the natural P-T paths of Naxos [*Martin 2004, Duchène et al. 2006*] or Tinos [*Parra et al., 2002*] to reject either model based

366 solely on thermo-barometric validation. However, in the fault propagator model, the behavior of
367 the two parts of the dome differs. Whilst rocks are exhumed from all depths close to the free-slip
368 boundary (dark gray, Figure 3f), within the strike-slip part of the dome, only high temperature
369 paths are sampled (light gray, Figure 3f).

370 The lineations measured in the MCCs of the Cyclades are reported on Figure 7a. The
371 outline of the modeled area is projected on the map so that the strikes of the lineation along the
372 North Cycladic Detachment System (green arrows, [*Jolivet et al., 2010*] are parallel to the
373 direction of stretching of the models. In that frame, the roughly north-south lineations of Naxos,
374 Paros and Ios (red arrows) [*Huet et al., 2009; Gautier et Brun, 1994*] form a 30-60° angle with
375 the direction of stretching of the model and the late lineations along the South Cycladic
376 Detachment System appear with intermediate strike (orange arrows, [*Isgleder et al., 2009*]). Not
377 only is the geographic repartition of the lineation in good agreement with the fault propagator
378 model (Figure 3c) but also the domes of Naxos, Paros and Ios fall actually in the class of domes
379 that are elongated in the direction of the lineation. This observation, together with the warmer P-
380 T paths in these domes and the migration to the south with time of from top-to-the-north-north-
381 east detachments to a top-to-the-south detachment [*Grasemann et al., 2012*], leads us to conclude
382 that the transtensional fault propagator model is a valid model for the formation of the Cyclades.
383 The obliquity of the lineation in the central Cyclades was previously attributed to a late phase of
384 solid rotation around a vertical axis [*Morris et Anderson, 1996*]. The sinistral fault propagator
385 model includes this obliquity into the continuum of the exhumation of the MCCs.

386 A strike-slip boundary of the Aegean-west Anatolian extensional system may have
387 started ~25 Ma ago [*Jolivet et al., 2012*]. Between 25 and 15 Ma, the total surface displacement

388 of the strike-slip boundary can be measured by the amount of extension in the northern Menderes
389 Massif resulting in some 50-60 km [*van Hinsbergen 2010*]. Until now, a lot of putative structures
390 have been proposed to accommodate strike-slip displacement in the area with different
391 orientation and kinematics [*Gautier and Brun 1994, Walcott and White,1998, Philipon et al.*
392 *2012*], however no large strike-slip structure has ever been clearly evidenced from field data or
393 seismic reflection data. Our numerical experiments show that the Naxos structure is better
394 explained as a transtensional structure rather than a purely extensional one. We argue that the
395 shape of the dome of Naxos [*Vanderhaeghe, 2004*, *Kruckenberg et al., 2011*] was acquired as it
396 plays the role of a lower crustal root of a strike-slip fault which was active in the Miocene times.
397 Whether the a-type shape of the dome of Naxos marks a local segment jump between the
398 Menderes massif and the Northern Cycladic Detachment System, or whether it is driven by
399 global geodynamics is a matter of debate which we cannot quantitatively assess based on the
400 results of our numerical experiments. However, to conclude on the Aegean dynamics, we would
401 like to propose a completely qualitative and conceptual, yet deliberately provocative model for
402 the formation of the splay fault that we imposed in the boundary condition of our preferred
403 Aegean model.

404 A tear within the Aegean slab is documented by Berk-Biryol *et al.* [*2011*] under western
405 Turkey and propagating along the Pliny and Strabo trenches south east of Crete and corresponds
406 today to a steep lateral gradient in trench retreat rate. The timing of the initiation of this tear is
407 debated. Pe-Piper et Piper [*2007*] and Jolivet et al. [*2009*] evaluate it at c.a. 20 Myr based on
408 adakites ages (Fig. 8 a. and b.) while van Hinsbergen et al. [*2010*] posit this tear is not older than
409 15 Myr based on palinspatic plate reconstruction. Reconstruction of the Aegean area [*Philippon*

410 *et al., 2012*] *show* that in the Miocene time, Anatolia and the Cyclades were probably further east
411 than the tears current location. The strike-slip wrenching recorded in the a-type structure of
412 Naxos could well be the lower crustal signature of a step fault accommodating the steep gradient
413 in slab retreat rate caused by the slab tear (Fig. 8c). Within that hypothesis, the tear in the slab
414 must initiate prior to 15 Myr, which corresponds to the late evolution of that dome [*Duchène et*
415 *al., 2006*].
416

417 ## 6 General discussion and conclusions

418 Previous models for the formation of non-cylindrical domes in the crust involved
419 components of normal shortening [*Thompson et al., 1997*], normal stretching [*Rey et al., 2011*]
420 or any complex poly-phased history which would include sequences of wrenching and folding or
421 a late refolding of a pre-existing b-type dome with a shortening direction normal to the direction
422 of extension [*Philipon et al 2012*]. All these equally valid models emphasize the non-uniqueness
423 of the solution when trying to reconstruct the kinematics from finite-strain markers. Here, we
424 show that the using a strike-slip fault propagator, or an extensional step-over in the boundary
425 conditions of numerical experiments, together with initial conditions which favor the formation
426 of MCCs, provides yet another valid alternative model for the emplacement of non-cylindrical
427 domes. However, the main point we would like to emphasize is that the presence of constrictive
428 ductile dome structures is not a sufficient argument to infer transpressive boundary conditions, or
429 far field shortening in the absence of a geochronological argument for a more complex poly-
430 phased deformation history, as was proposed in earlier models.

Comparing the numerical experiments with the Aegean, we propose an alternative model to the formation of the Cyclades and relate the N-S axis of the Naxos dome to a phase of transtension. A possible source for the transtension could be the presence of a tear in the Aegean slab, but other hypothesis such as a transfer fault between the Cyclades and the Menderes massif (Western Turkey) remain as a possibility. In any case, we argue that the elongation and the structure of the Naxos dome is an indicator that the dome acted as a strike-slip structure during its activity. An argument to support this model is that on the opposite side of the Mediterranean, a-type domes are clearly observed in the Betics [*Augier, 2005*] and are again aligned to a tear propagating in a slab [*Spackman and Wortel, 2004*].

The numerical experiments and conclusions drawn in this paper are directly applicable to MCCs other than those in the Aegean. However, given the availability of data from the Aegean, this region represents an excellent location to validate our ideas and verify our 3D thermo-mechanical models. Our numerical experiments constitute a first order study of the mode of 3D deformation of thickened crust. Each of these experiments would require a systematic parametric study varying rates of extension or shear, relative timing between the onset of shear and extension, depth of the viscosity step, length scale of the step over in order to be applied and validated with data in different geological settings and geodynamic contexts.

The aim of this paper was not to perform such parametric studies, but to open the door to alternative models and interpretations for the 3D ductile deformation of post-orogenic, relatively thickened crust. With our simulations, we have shown that it is possible to form folds in response to local constriction within extensional step-over between strike-slip faults (model 2, Figure 5). This model setup may well apply to the Red River Fault system along which many discontinuous

453 exhumed domes are out-cropping [*Leloup et al., 1995*]. Within this model, these domes would be
454 the mark of extensional step-over within a purely strike-slip system. Similarly, many of the
455 Variscan gneiss domes which form *en echellon* are usually interpreted as transpressional
456 structures (e.g. Pyrenees [*Denèle et al., 2007*]). Our model shows they could alternatively have
457 formed below an extensional step over within a purely strike-slip, large-scale kinematic
458 boundary conditions. The formation of these domes during the early stage of wrenching could
459 also participate in weakening the strike-slip faults by advecting hot/weak material within the
460 fault zone and locally reducing the effective elastic thickness of the fault zone as was proposed
461 by [*Chery, 2008*] to explain the GPS signal around the San Andreas Fault.

462 Further work is needed to completely understand the dynamics of strike-slip systems in
463 the ductile part of the crust, however as 3D thermo-mechanical modeling is now becoming
464 readily available, we can expect much progress to be made in the near future.

465 **APPENDIX**

466 ***A Computation of synthetic tectoglyphs***

467 The method used for the computation of the synthetic finite-strain field is an extension to
468 3D of a classical 2D method of Ramsay and Huber [*1987*]. The synthetic finite-strain field is
469 computed over a set of passive markers, which is meshed with tetrahedra. The schistosity and
470 lineation are computed for all tetrahedra in the following way.

471 Each tetrahedron is described by three non-colinear vectors that connect the four vertices.
472 These vectors are noted

473 $$\mathbf{a}_i = \left(x_i, y_i, z_i\right)^T, \quad i = 1,2,3 \tag{A.1}$$

474 in the initial (undeformed) configuration and

$$\mathbf{A}_i = \left(X_i, Y_i, Z_i\right)^T, \quad i = 1,2,3 \tag{A.2}$$

in the final (deformed) configuration, where the sign $^T$ designates the transpose operator. The two sets of vectors are gathered in two square matrices,

$$\mathbf{u} = \left(\mathbf{a}_1, \mathbf{a}_2, \mathbf{a}_3\right) \tag{A.3}$$

for the initial configuration and

$$\mathbf{U} = \left(\mathbf{A}_1, \mathbf{A}_2, \mathbf{A}_3\right) \tag{A.4}$$

for the final configuration.

The deformation matrix **D**, which relates the initial coordinates of the tetrahedron vectors to the final ones, links the matrices **u** and **U**:

$$\mathbf{U} = \mathbf{D}\mathbf{u} \quad \text{or} \quad \mathbf{D} = \mathbf{U}\mathbf{u}^{-1} \tag{A.5}$$

The finite strain ellipsoid is characterized by the eigenvalues $I_1 \le I_2 \le I_3$ and the corresponding eigenvectors $\mathbf{v}_1$, $\mathbf{v}_2$ and $\mathbf{v}_3$ of matrix

$$\mathbf{E} = \left(\mathbf{D}\mathbf{D}^{-1}\right)^{-1} \tag{A.6}$$

The major (resp. intermediate and minor) principal axis of the finite strain ellipsoid is parallel to $\mathbf{v}_1$ (resp. $\mathbf{v}_2$ and $\mathbf{v}_3$). The length of the major (resp. intermediate and minor) principal axis is $I_1^{1/2}$ (resp. $I_2^{1/2}$and $I_3^{1/2}$). Finally, the stretching lineation is a line parallel to $\mathbf{v}_1$ and the schistosity is a plane normal to $\mathbf{v}_3$. All these computations can be done using the script *tectoglyphs.m* provided with the manuscript.

***B Multi-grid in GALE***

Within GALE, the discretized Stokes equations are represented as follows;

$$\begin{pmatrix} \mathbf{K} & \mathbf{G} \\ \mathbf{D} & \mathbf{C} \end{pmatrix} \begin{pmatrix} \mathbf{u} \\ \mathbf{p} \end{pmatrix} = \begin{pmatrix} \mathbf{f} \\ \mathbf{h} \end{pmatrix} \tag{B.1}$$

The velocity pressure ($\mathbf{u},\mathbf{p}$) solution is obtained via Schur Complement Reduction. This entails applying a Krylov method to the Schur complement system

$$\left(\mathbf{D}\mathbf{K}^{-1}\mathbf{G} - \mathbf{C}\right)\mathbf{p} = \hat{\mathbf{f}}, \tag{B.2}$$

Where

$$\hat{\mathbf{f}} = \mathbf{D}\mathbf{K}^{-1}\mathbf{f} - \mathbf{h}\ , \tag{B.3}$$

to obtain the solution for $\mathbf{p}$. Following this, we apply another Krylov method to

$$\mathbf{K}\mathbf{u} = \mathbf{f} - \mathbf{G}\mathbf{p}\ , \tag{B.4}$$

in order to obtain the solution for $\mathbf{u}$. In GALE, the Schur complement system in (B.2) is solved using the Conjugate Gradient method. Iterations are terminated when the initial residual has been reduced by a factor of 1e5. Systems involving $\mathbf{K}$ are solved using FGMRES, using a stopping condition requiring that the initial residual be reduced by a factor of 1e6. The same Krylov method used to define the matrix-vector product in Eqn. (B.2) is used in both Eqn. (B.3) and Eqn. (B.4).

The performance of a Krylov method is strongly linked to the preconditioner used. The ideal preconditioner is both scalable and optimal; meaning that number of iterations required to reach convergence is constant as the finite element mesh is refined, and that the CPU time required to reach convergence scales linearly with the number of unknowns. For the system in Eqn. (B.2), GALE uses a preconditioner defined by the mass matrix, scaled by the inverse of the element-wise effective viscosity. For Q1-Q1 velocity-pressure spaces, this preconditioner has

been proven [*Grinevich and Olshanskii, 2009*] and demonstrated for geodynamic applications [*Geenen et al., 2009; Burstedde C. et al., 2009*] to produce iteration counts for the Schur complement system that are independent of the mesh resolution.

To achieve an overall optimal solution strategy for the complete Stokes solver, GALE employs a geometric multi-grid (GMG) preconditioner for systems of the form $\mathbf{K}\,\mathbf{y} = \mathbf{x}$. A geometric multi-grid preconditioner utilizes a hierarchical representation of the discrete operator $\mathbf{K}$. The simplest hierarchy contains two levels, consisting of $\mathbf{K}$ (fine level) and $\mathbf{K}_c$, a "coarse" grid operator which is defined on a coarser finite element mesh. In the classical multi-grid strategy, one removes high frequency components of the error in the solution by applying several iterations of an iterative method, such as Richardson+Jacobi or Richardson+Gauss-Seidel. Due to their properties, these methods are called "smoothers". Since only long wavelengths remain, the smoothed error can be represented on a coarser grid. The inter-grid transfer from the fine-to-coarse level is called "restriction". On the coarse grid, the exact error can be computed using a direct solver, as the coarse problem contains fewer degrees of freedom than the fine grid. The low-frequency errors on the coarse grid are transferred to the fine grid in order to correct the fine grid approximation for the low-frequency errors. The inter-grid transfer from the coarse-to-fine grid is called "prolongation". The smoother is also applied to the corrected fine grid approximation. We refer to Wesseling [*1992*], Briggs et al. [*2000*] and Trottenberg et al. [*2001*] for an in-depth discussion of multi-grid theory.

To obtain "text-book" efficiency multi-grid performance, the coarse grid operator has to be a meaningful approximation of the fine grid operator $\mathbf{K}$. For partial differential equations (PDEs) containing coefficients which are highly spatially variable (continuous or discontinuous)

537 and heterogeneous (e.g. viscosity), this is difficult within the framework of GMG. Primarily this
538 is due to the inability of the coarse grid to adequately resolve fine scale structures. Additionally,
539 in practice, the classical smoothers are found to be largely ineffective for problems which
540 possess large variations in coefficients. We note that in the instance of discontinuous
541 coefficients, if the coarse grid exactly resolves the coefficient jump, all the aforementioned
542 issues are eliminated. However, for most practical geodynamic models employing markers - this
543 scenario will rarely ever occur. In summary, the construction of the coarse grid operator and the
544 choice of the smoother are extremely important for the development of efficient GMG
545 preconditioners when they are applied to problems which exhibit large variations in coefficients.

546 In GALE, the restriction operation **R** is defined via bilinear interpolation between the fine and
547 coarse grid levels. The prolongation operator **P** is defined as the transpose of **R**. Galerkin coarse
548 grids operators are utilized on all levels (except the finest) in which the coarse grid operator is
549 constructed via $\mathbf{K}_c = \mathbf{R}\mathbf{K}\mathbf{R}^T$. This type of coarse grid can be interpreted as a projection of the
550 entire fine grid matrix onto the coarse grid. In general, practitioners often don't utilize Galerkin
551 coarse grid operators due to the programming complexity (particularly in parallel) of defining the
552 triple matrix product required. One alternative to Galerkin coarse grid operators is simply to
553 project the coefficients onto the coarse grid and re-discretize the original PDE. However, in
554 practical applications with large variations in coefficients, the Galerkin coarse grid operator
555 produces a much more robust preconditioner. In addition, the "smoother" used in GALE is a
556 fully-fledged Krylov method (FGMRES) equipped with a block Jacobi+ILU preconditioner. On
557 both the down and upward sweep in the multi-grid V-cycle, we apply 8 iterations of this Krylov
558 method. In contrast to the classical Richardson+(Jacoboi/Gauss Seidel/SOR) type smoothers, our

559 practical experience of using such "heavy" smoothers have proved to be robust when applied to
560 problems involving large variations in viscosity. Furthermore, on the coarsest grid level, we
561 utilize a fully parallel LU factorization SuperLU_Dist [*Xioye, 2005*]. All linear algebra, Krylov
562 methods and preconditioners are provided via PETSc v3.0 [*Balay et al., 2008*].

563 **ACKNOWLEDGMENTS**

564 GALE is software hosted by the Computational Infrastructure for Geodynamics (CIG) and
565 developed by CIG, Monash University and the Victorian Partnership for Advanced Computing
566 (VPAC). This research was supported by ANR EGEO. Author D.A.M. was supported by the
567 ETH Zurich Postdoctoral Fellowship Program. The topographic map was generated using
568 **http://www.geomapapp.org**

569 **REFERENCES CITED**

570 Allken V., R.S. Huismans and C. Thieulot (2011), *Three-dimensional numerical*
571 *modeling of upper crustal extensional systems,* J. Geophys. Res, 116, B10409

572 Augier R., P. Agard , P. Monié, L. Jolivet, C. Robin and G. Booth-Rea, (2005), P-T-D-t
573 retrograde evolution of the Nevado-Filabride complex (SE Spain) : new insights from in situ
574 40Ar/39 ages and metamorphic petrology, *Journal of Metamorphic Geology,* v. 23, p357-381

575 Balay S., W.D. Gropp, L.C. McInnes and B.F. Smith (2008), PETSc home page,
576 http://www.mcs.anl.gov/petsc

577 Block, L., and L. Royden (1990), Core complex geometries and regional scale flow in the
578 lower crust: *Tectonics*, v. 9, p. 557–567, doi: 10.1029/TC009i004p00557.

579 Bonev N., J.P. Burg and Z. Ivanov (2006),Mesozoic--Tertiary structural evolution of an
580 extensional gneiss dome—the Kesebir--Kardamos dome, eastern Rhodope (Bulgaria--
581 Greece),International Journal of Earth Sciences, v. 95, 2, pp318-340

582 Briggs W.L., V.E. Henson and S.F. McCormick(2000), A multigrid tutorial, seconde
583 edition, Society for Industrial and Applied Mathematics, Philadelphia, PA, USA, ISBN-10: 0-
584 89871-462-1, 193p.

585 Brun J.P, D. Sokoutis D. and J. Van den Driessche (1994), Analogue modeling of
586 detachment fault systems and core complexes, *Geology,* v. 22 p319-322

587 Brun, J.-P. (1999), Narrow rifts versus wide rifts: Inferences for the mechanics of rifting
588 from laboratory experiments, *Royal Society of London Philosophical Transactions*, ser. B, v.
589 357, p. 695–712.

590 Buck W.R. (1991), Modes of continental lithospheric extension, *Journal of Geophysical*
591 *Research*, v. 96, 20161–20.

592 Bullard E.C. (1936), Gravity measurements in East Africa, *Philosophical Transactions*
593 *of the Royal Society of London. Series A, Mathematical and Physical Sciences*, 235, 757, pp.445-
594 531

595 Burstedde C., O. Ghattas, G. Stadler,T. Tu and L.C. Wilcox (2009),Parallel scalable
596 adjoint-based adaptive solution of variable-viscosity Stokes flow problems, *Computational*
597 *Methods Appl. Mech. Engrg*, v. 198, pp.1691-1700

598 Berk Biryol C., S.L. Beck, G. Zandt, A. A. Özacar (2011), Segmented African
599 lithosphere beneath the Anatolian region inferred from teleseismic *P*-wave tomography,
600 *Geophysical Journal International*, DOI: 10.1111/j.1365-246X.2010.04910.x

601 Chéry J. (2008), Geodetic strain across the San Andreas Fault reflects elastic plate
602 thickness variations (rather than fault slip rate), *Earth and Planetary Science Letters*, 269, 3, pp
603 352-365

604 Choi E., L. Lavier and M. Gurnis (2008), Thermomechanics of mid-ocean ridge
605 segmentation, *Physics of the Earth and Planetary Interiors,* 171,1-4,pp 374-386

606 Denèle, Y., P. Olivier, G. Gleizes and P. Barbey (2007), The Hospitalet gneiss dome
607 (Pyrenees) revisited: lateral flow during Variscan transpression in the middle crust, *Terra Nova,*
608 19, 6, pp445-453

609 Duchène S., R. Assa, and O. Vanderhaeghe (2006), Pressure-temperature time evolution
610 of metamorphic rocks from Naxos (Cyclades, Greece): Constraints from thermobarometry and
611 Rb/Sr dating, *Geodynamica Acta*, 19, 301–321, doi:10.3166/ga.19.301-321

612 Echtler, H. and J. Malavieille (1990), Extensional tectonics, basement uplift and
613 Stephano-Permian collapse basin in a late Variscan metamorphic core complex (Montagne
614 Noire, Southern Massif Central), *Tectonophysics* , 177, 125–138.

615 Gaudemer, Y., C. Jaupart and P. Tapponnier (1988), Thermal control on post-orogenic
616 extension in collision belts, *Earth and planetary science letters,* 89, 48–62.

617 Gautier, P. and J.P. Brun (1994), Crustal-scale geometry and kinematics of late-orogenic
618 extension in the central Aegean (Cyclades and Ewia Island), *Tectonophysics,* 238, 399–424

619 Geenen T., M.U. Rehman, S.P. MacLachlan, G. Segal, C. Vuik, A.P. van den Berg and
620 W. Spaceman (2009), Scalable robust solvers for unstructured FE geodynamic modeling
621 applications: Solving the Stokes equation for models with large localized viscosity
622 contrasts,*Geochem. Geophys. Geosyst*, v.10, Q09002

623 Foster, D.A., P.T. Doughty, T.J. Kalakay, C.M Fanning, S. Coyner, W.C. Grice, and J.J.
624 Vogl, 2007, Kinematics and timing of exhumation of Eocene metamorphic core complexes along
625 the Lewis and Clark fault zone, northern Rocky Mountains, USA, in Till, A., Roeske, S.,
626 Sample, J., and Foster, D.A., eds., Exhumation along major continental strike-slip systems:
627 Geological Society of America Special Paper 434, p. 205-229, doi: 10.1130/2007.2343(10)

628 Gerya, T.V., L.L. Perchuk, D.D. van Reenen and C.A. Smit (2000), Two-dimensional
629 numerical modeling of pressure-temperature-time paths for the exhumation of some granulite
630 facies terrains in the Precambrian, *Journal of Geodynamics,* 30, 17–35.

631 Gerya T.V. (2010), Dynamical Instability Produces Transform Faults at Mid-Ocean
632 Ridges, *Science,* 329, 1047.

633 Grasemann B., D. A. Schneider, D. Stöckli and C. Iglesder (2012), Miocene bivergent
634 crustal extension in the Cyclades (Greece), *Lithosphere*, 4, 23-3, doi:10.1130/L164.1

635 Grinevich P.P. and M.A. Olshanskii (2009), An Iterative Method for the Stokes Type
636 Problem with Variable Viscosity, SIAM J. Sci. Comput., v.31,5,pp 3959-3978

637 Huet B., L. Labrousse and L. Jolivet (2009), Thrust or detachment? Exhumation
638 processes in the Aegean: insight from a field study on Ios (Cyclades, Greece), *Tectonics*,
639 28,TC3007.

640 Huet, B., L. Le Pourhiet, L. Labrousse, E. Burov and L. Jolivet (2011a), Post-orogenic
641 extension and metamorphic core complexes in a heterogeneous crust: the role of crustal layering
642 inherited from collision. Application to the Cyclades (Aegean domain), *Geophysical Journal*
643 *International,* DOI: 10.1111/j.1365-246X.2010.04849.x

644 Huet B., L. Le Pourhiet, L. Labrousse, E.B. Burov and L. Jolivet (2011b) Formation of
645 metamorphic core complex in inherited wedges: A thermomechanical modelling study*, Earth*
646 *and Planetary Science Letters,* 309, 3–4,p. 249-257

647 Howard K.A. and B.E. John (1987), Crustal extension along a rooted system of imbricate
648 low-angle faults: Colorado River extensional corridor, California and Arizona, Geological
649 Society, London, Special Publications, v. 28, 1,pp299-311

650 Hyndman, D. W. (1980). Bitterroot dome – Sapphire tectonic block, an example of a
651 plutonic core-gneiss-dome complex with its detached suprastructure. Cordilleran Metamorphic
652 Core Complexes. M. J. D. Crittenden, P. J. Coney and G. H. Davis, *Geological Society of*
653 *America Memoir*. 153: 427-443.

654 Iglseder C., Grasemann B., Schneider D.A., Petrakakis K., Miller C., Klötzli U.S.,Thöni
655 M., Zàmolyi A. and Rambousek C., 2009, I and S-type plutonism on Serifos (W-Cyclades,
656 Greece): Tectonophysics 473, 69–83

657 Jolivet, L., O. Beyssac, B. Goffé, D. Avigad and C. Lepvrier (2001), Oligo-Miocene
658 midcrustal subhorizontal shear zone in Indochina, *Tectonics,* 20, 46–57

659 Jolivet L., Famin V., Mehl C., Parra T., Aubourg C., Hébert R. and Philippot P., 2004,
660 Strain localization during crustal-scale boudinage to form extensional metamorphic domes in the
661 Aegean Sea: in *D.L. Whitney, C. Teyssier, 203 and C. S. Siddoway, Gneiss Domes in Orogeny,*
662 *GSA Special Papers* 380, pp 185–210

663 Jolivet L., C. Faccenna and C. Piromallo (2009), From mantle to crust: Stretching the
664 Mediterranean, *Earth and Planetary Science Letters*, 285, 198–209

665 Jolivet L., E. Lecomte, B. Huet , Y. Denèle , O. Lacombe , L. Labrousse, L. Le Pourhiet
666 and C. Mehl (2010), The North Cycladic Detachment System, *Earth and Planetary Science*
667 *Letters,* 289, 87–104

668 Jolivet L., C. Facenna, B. Huet et al. (2012), Aegean tectonics: strain localisation, slab
669 tearing and trench retreat, *Tectonophysics* doi: 10.1016/j.tecto.2012.06.011

670 Kruckenberg S.C., O. Vanderhaeghe, E.C. Ferré, C. Teyssier and D.L. Whitney (2011),
671 Flow of partially molten crust and the internal dynamics of a migmatite dome, Naxos, Greece,
672 *Tectonics,* 30, TC3001

673 Labrousse L., L. Jolivet, T.B. Andersen, P. Agard, R. Hébert, H. Maluski and U. Schärer
674 (2004), Pressure-temperature-time deformation history of the exhumation of ultra-high pressure
675 rocks in the Western Gneiss Region, Norway: in *D.L. Whitney, C. Teyssier, and C. S. Siddoway,*
676 *Gneiss Domes in Orogeny, GSA Special Papers,* 380, pp155–183

677 Lavier L., W. R. Buck and A.N. B. Poliakov (2000), Factors controlling normal fault
678 offset in an ideal brittle layer, *Journal of Geophysical Research*, 105, B10, pp. 23,431-23,442

679 Le Pichon, X., and J. Angelier (1981), The Aegean Sea, *Phil. Trans., R. Soc. London*,
680 300, 357-372.

681 Leloup P.H., R. Lacassin, P. Tapponnier, U. Schärer, Z. Dalai, L. Xiaohan, Z.
682 Liangshang, J. Shaocheng and P. T. Trinh (1995), The Ailao Shan-Red River shear zone
683 (Yunnan, China), Tertiary transform boundary of Indochina, *Tectonophysics*, 251, pp 3-84

684 Lemiale V., H.B. Mühlhaus, L. Moresi and J. Stafford, 2008, Shear banding analysis of
685 plastic models formulated for incompressible viscous flows, Physics of the Earth and Planetary
686 Interiors, 171,1-4,pp 177-186, 2008

687 Lister G.S. And S.L. Baldwin (1993), Plutonism and the origin of metamorphic core
688 complexes, *Geology*, 21, 607

689 Martin L., (2004). Signification des ages U-Pb sur zircon dans l'histoire métamorphique
690 de Naxos et Ikaria (Cyclades, Grèce). [Ph.D. Thesis], Nancy, Université Henri Poincaré Nancy

691 Martýnez-Martýnez J.M., J.I. Soto and J.C. Balanyá (2002), Orthogonal folding of
692 extensional detachments: structure and origin of the Sierra Nevada elongated dome (Betics, SE
693 Spain), *Tectonics,* 21, 1012

694 McKenzie D. and J. Jackson (2002), Conditions for flow in the continental crust,
695 *Tectonics,* 21, 1055

696 Moresi, L., F. Dufour and H.B. Mühlhaus (2003), A Lagrangian integration point finite
697 element method for large deformation modeling of viscoelastic geomaterials, *Journal of*
698 *Computational Physics*, 184, 476–497

699 Morris, A. and M. Anderson (1996), First palaeomagnetic results from the Cycladic
700 Massif, Greece, and their implications for Miocene extension directions and tectonic models in
701 the Aegean, *Earth and planetary science letters*, 142, 397–408

702 Parra T., O. Vidal and L. Jolivet (2002), Relation between the intensity of deformation
703 and retrogression in blueschist metapelites of Tinos Island (Greece) evidenced by chlorite-mica
704 local equilibria, *Lithos*, 63, 41–66

705 Pe-Piper G. and D.J.W. Piper (2007), Neogene backarc volcanism of the Aegean: New
706 insights into the relationship between magmatism and tectonics, *GSA Special Papers,* v. 418, p.
707 17-31 doi: 10.1130/2007.2418(02)

708 Philippon M., J.P. Brun and F. Gueydan (2012) Deciphering subduction from exhumation
709 in the segmented Cycladic Blueschist Unit (Central Aegean, Greece), *Tectonophysics*, v. 524–
710 525, p116-134, ISSN 0040-1951, 10.1016/j.tecto.2011.12.025.

711 Ramsay J.G and M.I. Huber, 1983, The Techniques of Modern Structural Geology
712 Volume 1: Strain Analysis, Academic Press London, New York, 307p.

713 Rey, P.F., C. Teyssier and D.L. Whitney (2009), Extension rates, crustal melting, and
714 core complex dynamics, *Geology*, 37, 391

715 Rey, P.F., C. Teyssier, S.C. Kruckenberg and D.L. Whitney (2011), Viscous collision in
716 channel explains double domes in metamorphic core complexes, *Geology,* 39, 387

717 Reynolds, S. J. and J. E. Spencer (1985), Evidence for large-scale transport on the
718 Bullard detachment fault, west-central Arizona., *Geology,* 13, 353-356.

719 Ring U., J. Glodny, T. Will and S. Thomson (2010), The Hellenic subduction system:
720 high-pressure metamorphism, exhumation, normal faulting, and large-scale extension, *Annual*
721 *Review of Earth and Planetary Sciences,* 38, p45–76

722 Spakman, W. and R. Wortel (2004), A tomographic view on Western Mediterranean
723 geodynamics, *The TRANSMED Atlas, The Mediterranean Region from Crust to Mantle,* pp31-52

724 Spadini G. and Y. Podladchikov (1996), Spacing of consecutive normal faulting in the
725 lithosphere: A dynamic model for rift axis jumping,Tyrrhenian Sea, *Earth and Planetary Science*
726 *Letters*, 144, p. 21–34

727 Thompson A.B., K. Schulmann and J. Jezek (1997) , Thermal evolution and exhumation
728 in obliquely convergent (transpressive) orogens, *Tectonophysics,* 280, 171–184

729 Tirel C., J.P Brun and E. Burov (2008), Dynamics and structural development of
730 metamorphic core complexes, *Journal of Geophysical Research,* 113, B04403

731 Tirel, C., P. Gautier, D. J. J. van Hinsbergen, and M. J. R. Wortel (2009), Sequential
732 development of interfering metamorphic core complexes: Numerical experiments and
733 comparison with the Cyclades, Greece, in: *Collision and Collapse at the Africa-Arabia-Eurasia*
734 *Subduction Zone, edited by D. J. J. van Hinsbergen, M. A. Edwards, and R. Govers, Geol. Soc.*
735 *Spec. Publ.*, 311, 257–292, doi:10.1144/SP311.10.

736 Trottenberg U., C.W. Oosterlee and A. Schüller (2001), Multigrid, Academic Press,
737 Inc.,ISBN 0-12-701070-X, 650p.

738 Van Hinsbergen, D.J.J., N. Kaymakci, W. Spakman and T.H. Torsvik (2010),
739 Reconciling the geological history of western Turkey with plate circuits and mantle tomography,
740 *Earth Planet. Sci. Lett., **297**, 674-686*

741 Vanderhaeghe O. and C. Teyssier (2001), Partial melting and flow of orogens,
742 *Tectonophysics,* 342, 451-472.

743 Vanderhaeghe O. (2004), Structural development of the Naxos migmatite dome, *in*
744 *Gneiss Domes in Orogeny, edited by D. L. Whitney et al., Spec. Pap. Geol. Soc. Am.*, 318, 211–
745 227, doi:10.1130/0-8137-2380-9.211.

746 Vening Meinesz F.A. (1950), Les graben africains, résultat de compression ou de tension
747 dans la croûte terrestre, *Inst. R. Coll. Belge Bull,* 21,pp 539-552

748 Walcott CR and SH. White (1998), Constraints on the kinematics of postorogenic
749 extension imposed by stretching lineations in the Aegean region, *Tectonophysics,* 298, pp.155–
750 175

751 Wesseling P. (1992), An Introduction to Multigrid Methods, John Wiley &
752 Sons,Chichester, United Kingdom, ISBN-10 1930217080, 296p.

753 Wijns C., R. Weinberg, K. Gessnerb and L. Moresi (2005), Mode of crustal extension
754 determined by rheological layering, *Earth and Planetary Science Letters,* 236, p. 120– 134

755 Xiaoye S.L. (2005), An overview of SuperLU: Algorithms, implementation, and user
756 interface,ACM Trans. Math. Softw., v.31, 3,pp. 302-325

757 Yamato P., P. Agard, E. Burov, L. Le Pourhiet, L. Jolivet, and C. Tiberi (2007) Burial
758 and exhumation in a subduction wedge: Mutual constraints from thermomechanical modeling
759 and natural P-T-t data (Schistes Lustrés, western Alps), J*ournal of Geophysical Research*, 112,
760 B07410, doi:10.1029/2006JB004441

761 **TABLES**

762 **Table 1:** ***Model parameters***

| Notation/Unit | Lower crust | Upper crust | Mantle |
|---|---|---|---|
| $\eta_0$ (Pa.s) | $10^{26}$ | $10^{26}$ | $10^{26}$ |
| $\theta$ ($°C^{-1}$) | 0.035 | 0.020 | 0.012 |
| $\eta_{eff}$ at 300°C (Pa.s) | $3x10^{21}$ | $2x10^{23}$ | $3x10^{24}$ |
| $\eta_{eff}$ at 700°C (Pa.s) | $10^{19}$ | $8x10^{19}$ | $2x10^{22}$ |
| $\eta_{eff}$ at 1100°C (Pa.s) | $10^{19}$ | $10^{19}$ | $2x10^{19}$ |
| Co (Pa) | $2x10^{7}$ | $2x10^{7}$ | $2x10^{3}$ |
| $Co_{inf}$ (Pa) | $2x10^{7}$ | $2x10^{7}$ | $2x10^{3}$ |
| $\varphi$ (°) | 30 | 30 | 15 |
| $\varphi_{inf}$ (°) | 10 | 10 | 15 |
| $\alpha$ ($K^{-1}$) | $3x10^{-5}$ | $3x10^{-5}$ | $3x10^{-5}$ |
| $\chi$ ($m^2s^{-1}$) | $10^{-6}$ | $10^{-6}$ | $10^{-6}$ |
| $\rho$ (kg $m^{-3}$) | 2800 | 2800 | 3300 |

763

764 **Table 2:** ***Scaling used for computations***

| Notation/Unit | Model | Nature (SI) | Scaling (SI) |
|---|---|---|---|
| Velocity [$LT^{-1}$] | $10^{5}$ | $10^{-10}$ | $10^{-15}$ |
| Distance [L] | 1 | $10^{5}$ | $10^{5}$ |
| Time [T] | $10^{-6}$ | $10^{14}$ | $10^{20}$ |
| Viscosity [$ML^{-1}T^{-1}$] | $10^{-4}$ | $10^{19}$ | $10^{23}$ |
| Stress [$ML^{-1}T^{-2}$] | $10^{3}$ | $10^{6}$ | $10^{3}$ |
| Density [$ML^{-3}$] | 1 | $10^{3}$ | $10^{3}$ |
| Gravity [$LT^{-2}$] | $10^{6}$ | 10 | $10^{-5}$ |
| Thermal diffusivity [$L^{2}T^{-1}$] | $10^{4}$ | $10^{-6}$ | $10^{-10}$ |
| Temperature [°C] | 1 | 1 | 1 |

765

766 **FIGURE CAPTIONS**

767 Figure 1: On the right, a 3D sketch (modified from Jolivet et al. [*2004*]) illustrates two classes of
768 domes. On the left, a sketch illustrates the stereo-plot projections of the lineation (L) and
769 foliation (S) for the two kinds of dome. In the a-type dome, constriction is important and
770 the foliation is folded with axis aligned with the direction of stretching. In the b-type
771 dome, the foliation is folded with an axis normal to the direction of extension. The a-type
772 domes are not cylindrical and cannot be modeled in 2D.

773 Figure 2 : a. Initial geotherm is linear with a thermal gradient of 17°C/km down to the 1300°C
774 isotherm and constant deeper; b. Lithostratigraphic column with density u.c., l.c. and m.
775 stands for upper crust, lower crust and mantle respectively; c. Yield strength envelopes
776 drawn in extension for a background strain rate equal to the mean strain rate (black line,
777 $1.5x10^{-15}$ $s^{-1}$) and ten times the mean strain rate (red line, $1.5x10^{-14}$ $s^{-1}$).

778 Figure 3: Kinematic boundary conditions, surface deformation and topography with equidistance
779 of 100 m for the three models after 12 Myr evolution. The black, gray, cyan and pink line
780 outline respectively the right, left, back and front face of the model. Brown lines initially
781 formed squares. a. Model 1 assumes cylindrical extension; b. Model 2 corresponds to a
782 60 km wide extensional step-over; c. Model 3 represents a transtensional fault
783 propagator.

784 Figure 4: Results for cylindrical extension (Model 1). a. Internal deformation of the model
785 outlined by cross-sections across the material points and by tubes representing the
786 stretching lineation (maximum stretching axis of the finite strain tensor). The tubes are
787 colored by their strike with color scale represented in b. where gray indicates when the

788 lineation is aligned with the direction of stretching imposed at the boundary of the model;
789 b. Stereo-plot representation of the lineation (red) and the foliation (black) for all the
790 tracers located at less than 8 km depth after 12 Myr of simulation; c. Synthetic P-T path
791 for the same tracers as those represented in the stereo-plot in b. Initial and final thermal
792 gradient in blue and yellow respectively. The final thermal gradient is constrained
793 assuming the line goes though 0° at the surface.

794 Figure 5: Results for extensional step over (Model 2), legend is the same as for Figure 4

795 Figure 6: Results for transtensional fault propagator (Model 3), legend is the same as for Figure 4

796 Figure 7: a. Topographic map of the Cyclades with outline of the Cycladic MCCs (purple area),
797 as well as stretching lineations and sense of shear (arrows drawn after Martin [2004],
798 Huet et al. [*2009*], Iglseder et al. [*2009*], Jolivet et al. [*2010*] and Ring et al. [*2011*]). The
799 different colors outline different provinces associated with typical strikes using the same
800 color scale as in Fig 4. The modeled area is reported with white dashed lines, black boxes
801 denotes where the cylindrical part and non-cylindrical part were sampled in the model 3
802 to produce the part c and d of the figure; b: Geological sketch representing the main
803 structural features of model 3; c: The blue and magenta lines are the natural P-T paths of
804 Tinos [*Parra et al., 2002*] and Naxos [*Duchène et al., 2006*] respectively. Light and dark
805 gray lines denote paths located within non-cylindrical and cylindrical part of model 3 (see
806 a); d: Stereo-plot of the stretching lineation (red) and pole of the foliation (black) in the
807 cylindrical (left) and non-cylindrical (right) part of model 3 oriented in the same frame as
808 the map in a. The cylindrical part is a typical b-type dome while the non-cylindrical part

809 resembles an a-type dome with a non negligible number of lineation oriented N-S like in
810 Naxos.
811
812 Figure 8: a and b Paleogeographic reconstructions of the Cyclades and slab tear simplified from
813 [*Jolivet et al., 2009*], adakite from [*Pe-Piper and Piper, 2007*]; c. Sketch indicating how
814 a slab tear could be responsible for the strike component imposed at the boundary of
815 model 3.

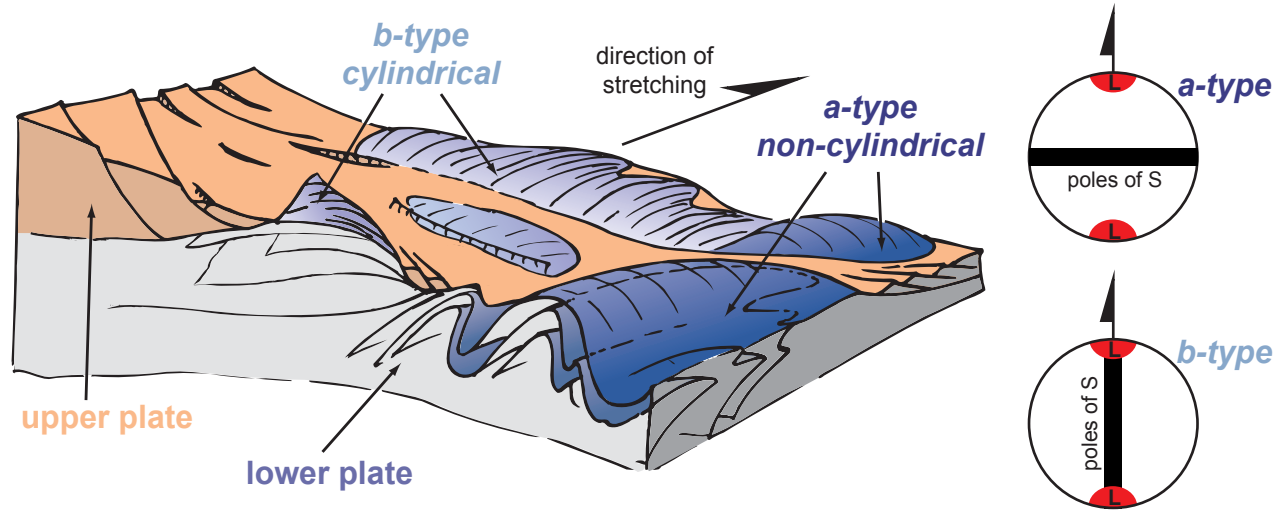


Figure 1: On the right, a 3D sketch (modified from Jolivet et al. [2004] ) illustrates two classes of domes. On the left, a sketch illustrates the stereo-plot projections of the lineation (L) and foliation (S) for the two kinds of dome. In the a-type dome, constriction is important and the foliation is folded with axis aligned with the direction of stretching. In the b-type dome, the foliation is folded with an axis normal to the direction of extension. The a-type dome are not cylindrical and can not be modeled in 2D.

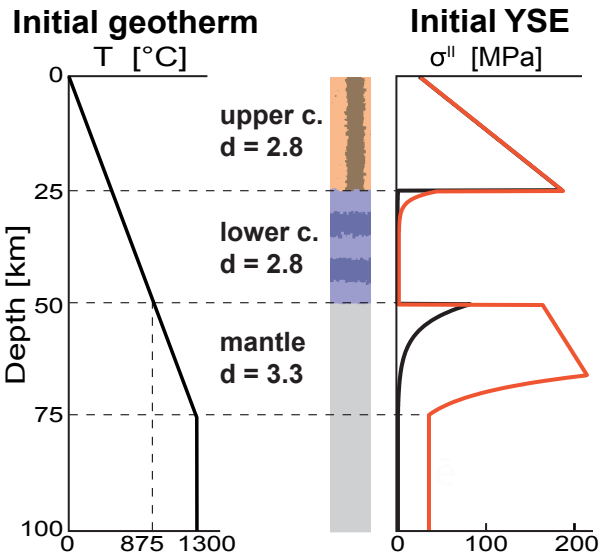


Figure 2 : a. Initial geotherm is linear with a thermal gradient of 17°C/km down to the 1300°C isotherm and constant deeper; b. lithostratigraphic column with density u.c., l.c. and m. stands for upper crust, lower crust and mantle respectively c. Yield Strength Envelopes drawn in extension for a background strain rate equal to the mean strain rate (black line, 1.5x10-15 s-1) and ten times the mean strain rate (red line, 1.5x10-14 s-1).

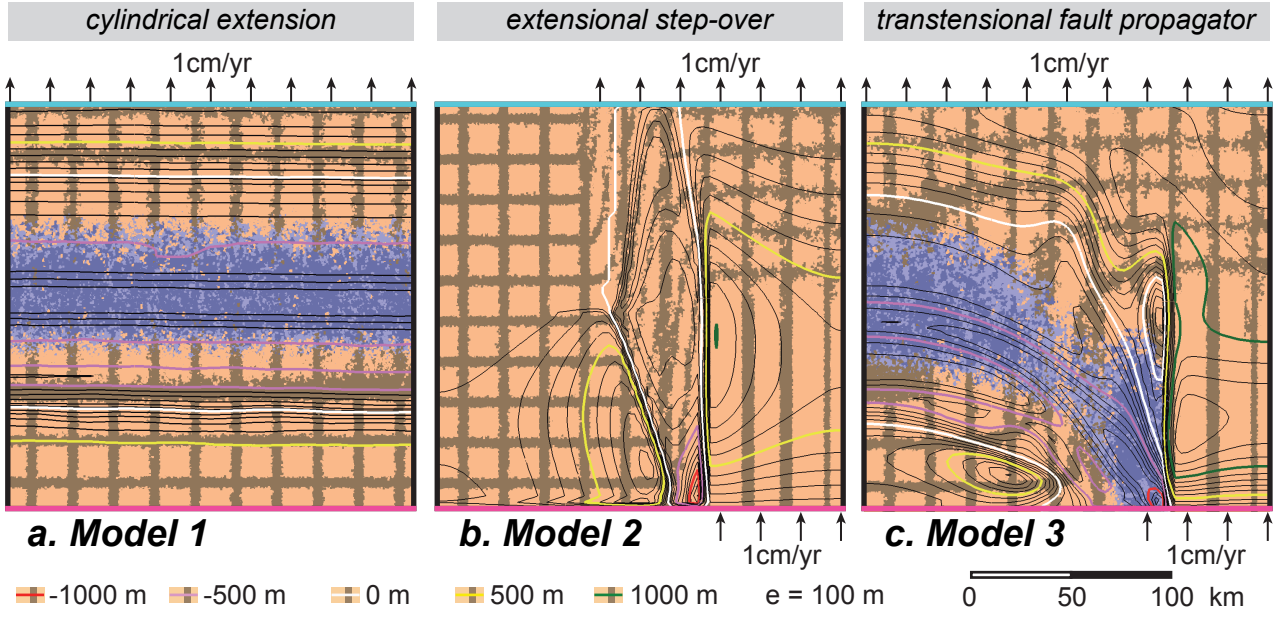


Figure 3: Kinematic boundary conditions, surface deformation and topography with equidistance of 100m for the 3 models after 12 Myr evolution. Brown lines initially formed squares. a. Model 1 assumes cylindrical extension b. Model 2 corresponds to a 60 km wide extensional step over c. Model 3 represents a trans-tensional fault propagator.

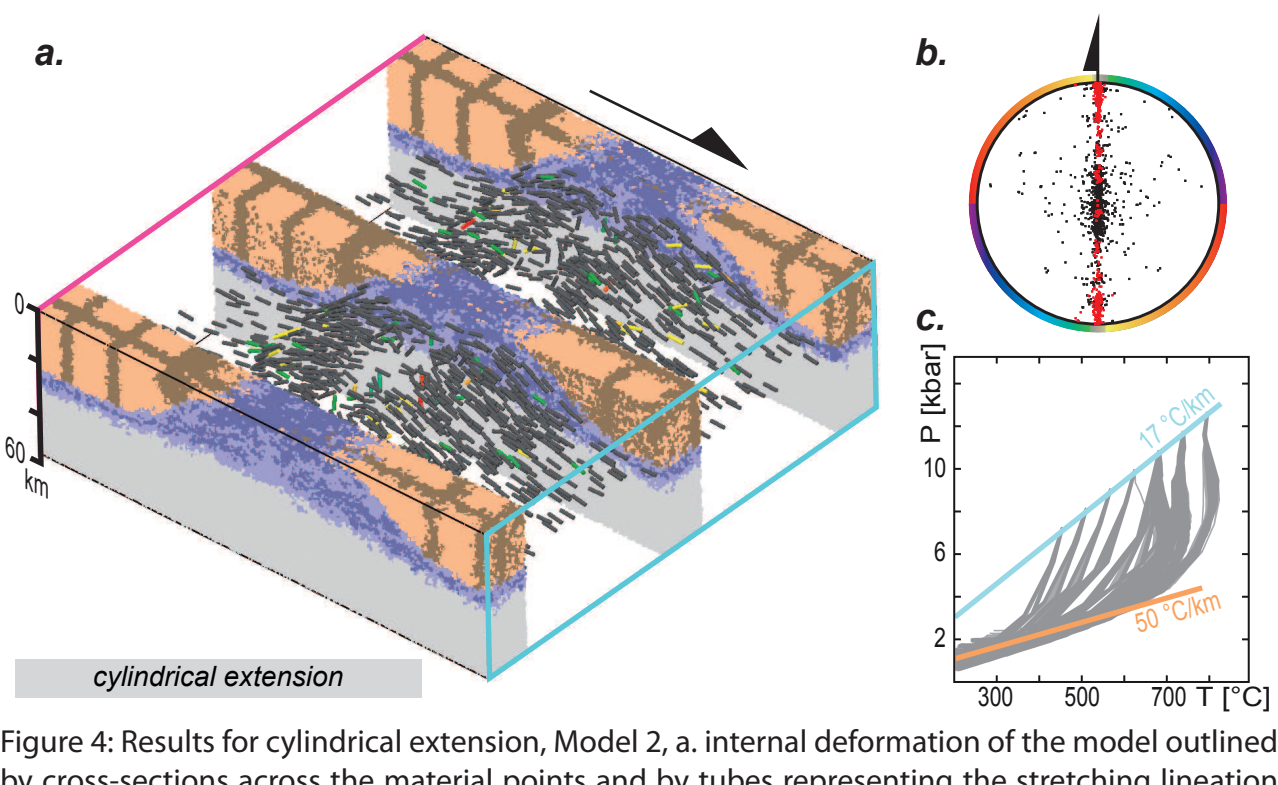


Figure 4: Results for cylindrical extension, Model 2, a. internal deformation of the model outlined by cross-sections across the material points and by tubes representing the stretching lineation (maximum stretching axis of the finite strain tensor). The tubes are colored by their strike with color scale represented in b. gray being used when the lineation is aligned with the direction of stretching imposed at the boundary of the model; b. Stereo-plot representation of the lineation (red) and the foliation (black) for all the tracers located at less than 8km depth after 12 Myr of simulation; c. Synthetic PT path for the same tracers as those represented in the stereo-plot in b Initial and final thermal gradient in blue and yellow respectively. The final thermal gradient is constrained assuming the line goes though 0° at the surface.

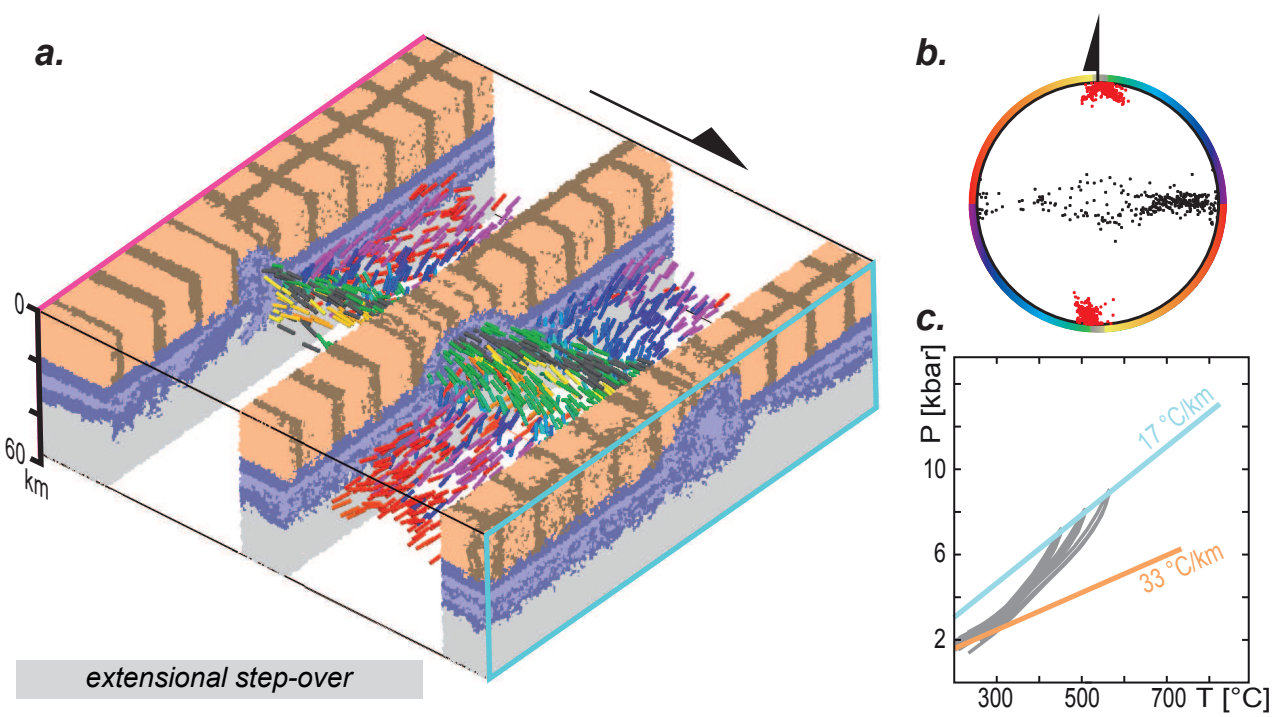


Figure 5: Results for extensional step over, Model 2, legend is the same as for Figure 4

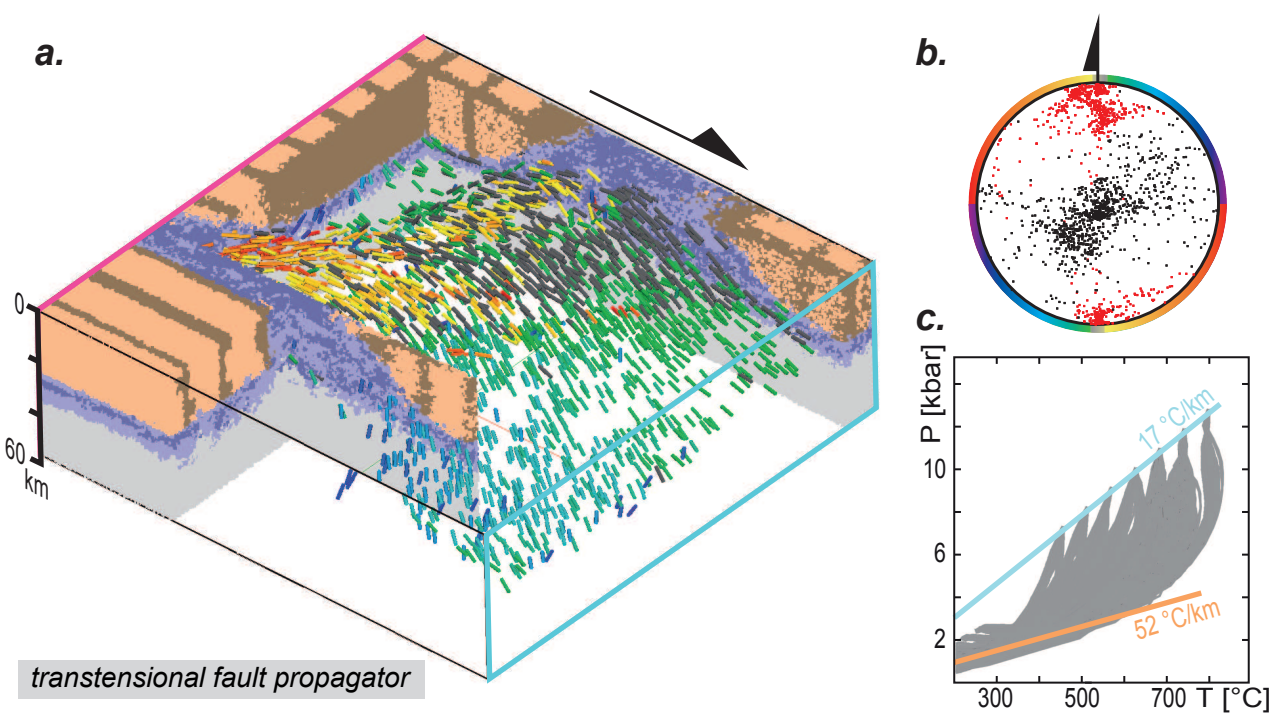


Figure 6: Results for trans-tensional fault propagator, Model 3, legend is the same as for Figure 4

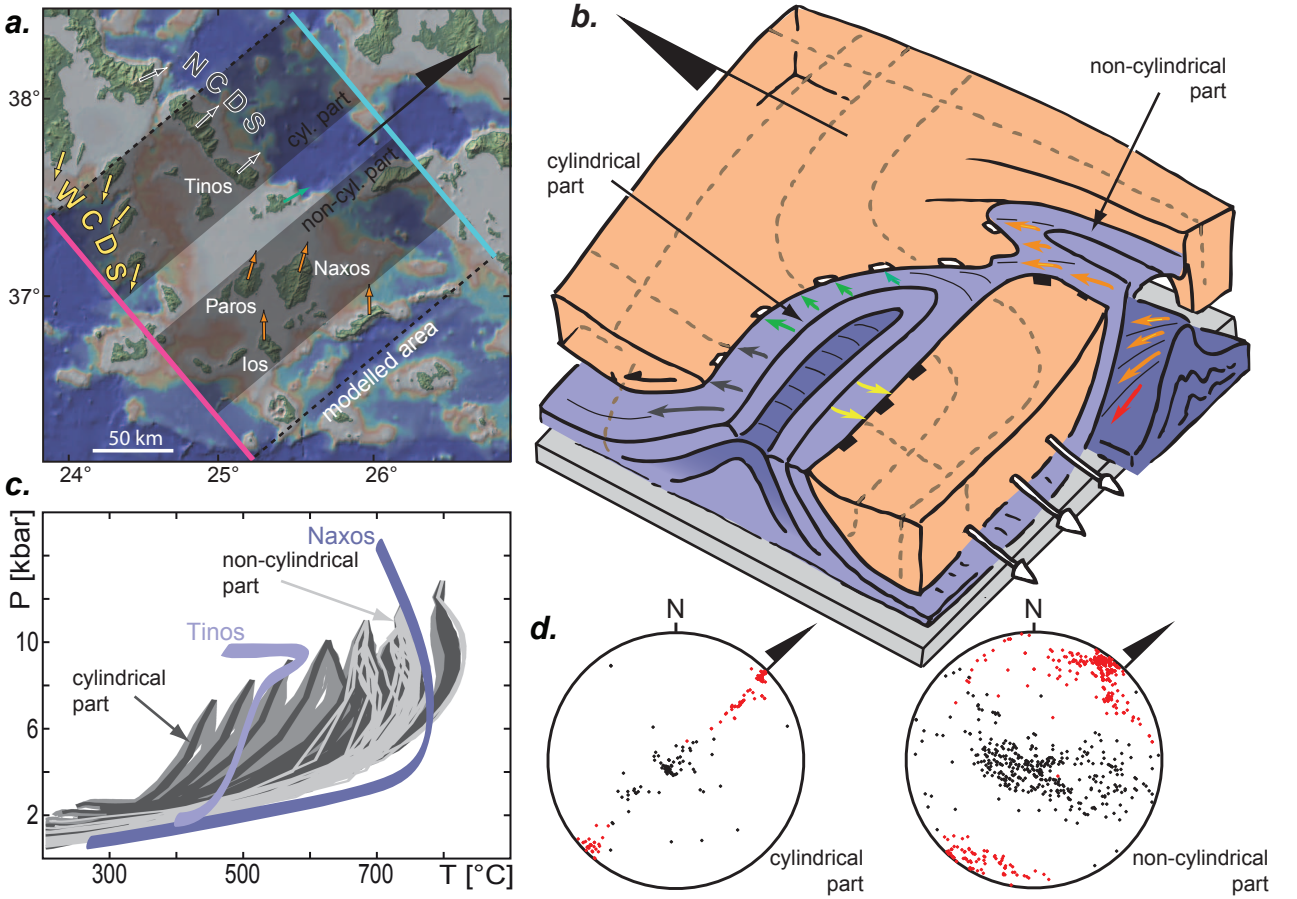


Figure 7: a. Topographic map of the Cyclades with outline of the Cycladic MCCs (purple area), as well as stretching lineations and sense of shear (arrows drawn after Martin [2004], Huet et al. [2009], Iglseder et al. [2009], Jolivet et al. [2010] and Ring et al. [2011]). The different colors outline different provinces associated with typical strikes with a similar color code as in Fig 4. The modeled area is reported with white dashed lines, black boxes denotes where the cylindrical part and non cylindrical part where sampled in the model 3 to produce the part c and d of the figure; b: geological sketch representing the main structural features of model 3; c: the blue and magenta lines are the natural P-T paths of Tinos [Parra et al., 2002] and Naxos [Duchène et al., 2006] respectively. Light and dark gray lines denote paths located within non-cylindrical and cylindrical part of model 3 (see a); d: stereo-plot of the stretching lineation (red) and pole of the foliation (black) in the cylindrical (left) and and non-cylindrical (right) part of model 3 oriented in the same frame as the map in a. The cylindrical part is a typical b-type dome while the non cylindrical part resemble a-type with non negligible number of lineation oriented N-S like in Naxos.

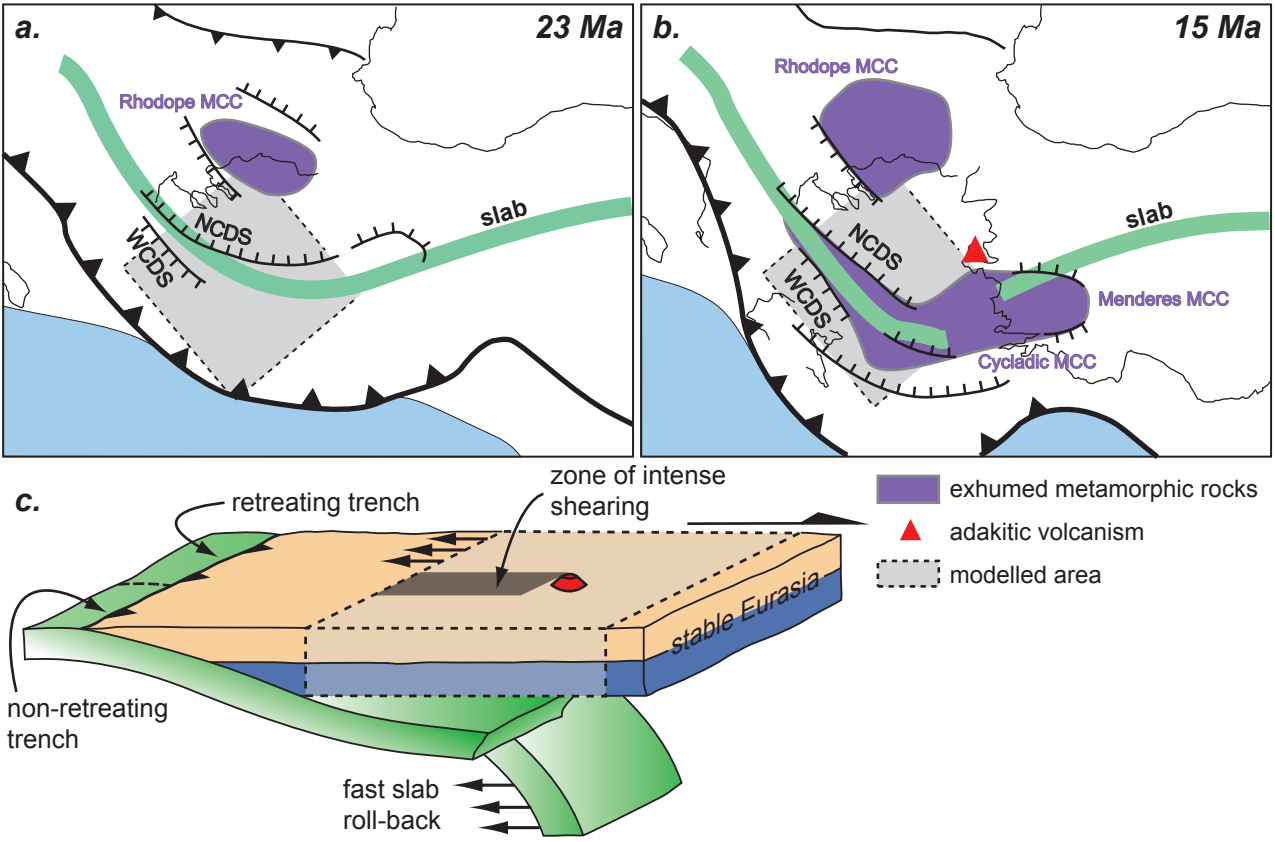


Figure 8: a and b paleogeographic reconstructions of the Cyclades and slab tear simplified from [Jolivet et al., 2009], adakite from [Pe-Piper and Piper, 2007] c: sketch presenting how a slab tear could be responsible for the strike component imposed at the boundary of model 3.